Extreme events and non-Kolmogorov −5/3 spectra in turbulent flows behind two side-by-side square cylinders

Yi Zhou[1,†], **Koji Nagata**[2], **Yasuhiko Sakai**[3] **and Tomoaki Watanabe**[2]

[1]School of Energy and Power Engineering, Nanjing University of Science and Technology, Nanjing 210094, PR China

[2]Department of Aerospace Engineering, Nagoya University, Nagoya 464-8603, Japan

[3]Department of Mechanical Systems Engineering, Nagoya University, Nagoya 464-8603, Japan

Turbulent flows behind two side-by-side square cylinders with three different gap ratios, namely, $L_d/T_0 = 4$, 6 and 8 (L_d is the separation distance between two cylinders and T_0 is the cylinder thickness) are investigated by using direct numerical simulations. Depending on the strength of the gap flow, the three cases can generally be characterized into two regimes, one being the weak gap flow regime and the other being the robust gap flow regime. The wake-interaction length scale can only be applied to characterize the spatial evolution of the dual-wake flow in the robust gap flow regime. And only in this regime can the so-called 'extreme events' (i.e. non-Gaussian velocity fluctuations with large flatness) be identified. For the case with $L_d/T_0 = 6$, two downstream locations, i.e. $X/T_0 = 6$ and 26, at which the turbulent flows are highly non-Gaussian distributed and approximately Gaussian distributed, respectively, are analysed in detail. A well-defined −5/3 energy spectrum can be found in the near-field region (i.e. $X/T_0 = 6$), where the turbulent flow is still developing and highly intermittent and Kolmogorov's universal equilibrium hypothesis does not hold. We confirm that the approximate −5/3 power law in the high-frequency range is closely related to the occurrences of the extreme events. As the downstream distance increases, the velocity fluctuations gradually adopt a Gaussian distribution, corresponding to a decrease in the strength of the extreme events. Consequently, the range of the −5/3 power law narrows. In the upstream region (i.e. $X/T_0 = 6$), the second-order structure function exhibits a power-law exponent close to 1, whereas in the far downstream region (i.e. $X/T_0 = 26$) the expected 2/3 power-law exponent appears. The larger exponent at $X/T_0 = 6$ is related to the fact that fluid motions in the intermediate range can directly 'feel' the large-scale vortex shedding.

Key words: turbulence simulation, turbulence theory

1. Introduction

The flow past a slender cylinder (either circular or square one) is one of the most important free shear flows (Williamson 1996). It has long been known that Kármán's

† Email address for correspondence: yizhou@njust.edu.cn

vortex street can be generated if the Reynolds number is larger than a certain value. Compared with a single wake, the flows downstream of two or more slender bluff bodies are much more complicated (Kolář, Lyn & Rodi 1997; Zhou *et al.* 2001; Alam, Zhou & Wang 2011; Alam & Zhou 2013; Alam, Bai & Zhou 2016), in which the interactions of vortex streets are involved. Such flows can be encountered in a wide variety of practical engineering situations (e.g. heat exchangers, offshore platforms, bridge piers, wind farms). Therefore, the flow behind two side-by-side cylinders is a subject of great practical importance.

The flow behind two square cylinders is largely decided by the gap ratio L_d/T_0, where L_d is the separation distance between two cylinders and T_0 is the cylinder thickness. Previous experimental studies (Alam *et al.* 2011; Alam & Zhou 2013) suggested that for the dual-wake flows with different gap ratios L_d/T_0, different flow patterns can be identified. Grid-generated turbulence, in the upstream of which wake interactions occur, has been intensively investigated over the past several decades. By using the scaling law of a single wake (Townsend 1956), Mazellier & Vassilicos (2010) introduced the wake-interaction length scale with $X_* = L_d^2/T_0$ to normalize the streamwise distance from the grid element X. It was demonstrated that when the downstream distance X is normalized by X_*, various centreline statistics of the turbulence behind grid elements with different mesh sizes can be collapsed together (Mazellier & Vassilicos 2010; Gomes-Fernandes, Ganapathisubramani & Vassilicos 2012; Nagata *et al.* 2013; Nagata *et al.* 2017). Note that immediately behind a grid element, four wakes are generated and they interact with their neighbouring wakes. Compared with the grid-generated turbulence, the turbulent flow behind two side-by-side cylinders is a more fundamental problem related to wake interactions. Therefore the simplest assessment of the wake-interaction length scale can be achieved by investigating the dual-wake flow behind two square cylinders.

The turbulent flow in the immediate vicinity of a grid element has recently received considerable attention (Hurst & Vassilicos 2007, Valente & Vassilicos 2011, Gomes-Fernandes, Ganapathisubramani & Vassilicos 2014; Zhou *et al.* 2015, 2016*a*). One interesting finding, which has been extensively reported (Mazellier & Vassilicos 2010, Nagata *et al.* 2013; Zhou *et al.* 2014*a*,*b*, 2016*b*; Laizet, Nedić & Vassilicos 2015*a*,*b*; Paul, Papadakis & Vassilicos 2017) is that turbulent flow in the lee of the grid can be highly intermittent with non-Gaussian distributions of the velocity fluctuations. The profile of the probability density function (PDF) of the streamwise velocity fluctuations u' is much wider than the corresponding Gaussian distribution, indicating a large probability of occurrence of the extreme events (in some papers (Mazellier & Vassilicos 2010; Laizet *et al.* 2015*b*) also called intense events). Moreover, the skewness of u' in the upstream region is negative, revealing that the PDF profiles are negatively skewed (Mazellier & Vassilicos 2010; Zhou *et al.* 2014*a*; Laizet *et al.* 2015*b*; Paul *et al.* 2017). A less noticed observation (Laizet *et al.* 2015*b*; Zhou *et al.* 2016*b*; Paul *et al.* 2017) is that the extreme events appear to be closely related to the formation of the $-5/3$ scaling power law.

It is well known that a class of flows called 'free shear flows' including turbulent jets and wakes share some important turbulence characteristics, for example, self-similarity of various one-point statistics and the existence of very thin/sharp layers separating the free shear flows from their surrounding non-turbulent ambient flows (da Silva *et al.* 2014). Interestingly, a recent numerical study by Zhou *et al.* (2018) demonstrated that the extreme events can also be found in the merging regions of dual-parallel jet flows. However, the extreme events found in the merging region are quite different from those in the grid-generated turbulence. The corresponding probability distribution in dual-plane jet flows is positively skewed, not the contrary.

In light of the above mentioned publications, the present paper tries to find answers to the following two questions:

(1) In both grid-generated turbulence and dual-plane jet flows, extreme events can be found. The first question that naturally arises is whether the extreme events can also be found in the flow behind two square cylinders with different gap ratios? If the answer is yes, then what physical mechanisms are responsible for the extreme events? Moreover, it is of equal importance to clarify the characteristics of the extreme events.

(2) Previous studies suggested that the extreme events appear to be closely related to the appearance of the −5/3 scaling power law. A question then arises concerning the intimate relationship between the occurrence of the extreme events and the well-defined −5/3 energy spectra. More specifically, how do the extreme events contribute to the appearance of the −5/3 scaling law? The observation that the −5/3 scaling law can be found in the region where the extreme events occur is not in accord with Kolmogorov's prediction. Note also that according to the Kolmogorov phenomenology, in the so-called 'inertial subrange' the second-order structure function in real space is expected to acquire a power law with an exponent close to 2/3 when the corresponding −5/3 energy spectrum can be identified. The characteristics of the second-order structure function in the flow region where the extreme events can be identified is consequently another interesting topic and is of particular importance.

The organization of the rest of the paper is as follows. Section 2 presents the details about the simulation conditions and numerical method. In §3, the discussion on the wake-interaction scale is given and the statistical results concerning the extreme events are presented. In §4, the relationship between the extreme events and the −5/3 energy spectra is explored. The spatial evolution of the corresponding second-order structure function is also discussed. Finally, the main conclusions and remaining issues, which should be addressed in future, are listed in §5.

2. Numerical details

We perform direct numerical simulations (DNSs) of the flow behind two side-by-side square cylinders with three different gap ratios, i.e. $L_d/T_0 = 4$, 6 and 8. The details of the three cases are summarized in table 1. A schematic view of the computational domain is presented in figure 1 along with the coordinate system. Two identical parallel square cylinders are placed at the downstream streamwise location $X_{bar}/T_0 = 8$ from the inlet. The inlet length X_{bar} is comparable to those in previous numerical investigations of grid-generated turbulence (Laizet *et al.* 2015*a*,*b*; Paul, Papadakis & Vassilicos 2017, 2018). Note also that the blockage ratios are 7.1 %, 6.7 % and 5.9 %, which are much smaller than those in previous studies (i.e. 19 % in Laizet *et al.* (2015*a*,*b*) and 20 % in Paul *et al.* (2017, 2018)). It might be worth mentioning that for the studies mentioned (Laizet *et al.* 2015*a*,*b*; Paul *et al.* 2017, 2018), the numerical results are reported to be in good accord with the corresponding experimental results. Thus, our choice of X_{bar} is expected to be sufficiently large. The inlet Reynolds number $Re_{T_0} = U_{in}T_0/\nu$, with ν being viscosity, is 2500 for all three cases. A uniformly distributed velocity U_{in} is imposed at the inlet and a convective condition is applied at the outlet. The periodic boundary conditions are adopted in the Y and Z directions. The nodes are uniformly distributed in all three directions.

The immersed boundary method (Parnaudeau *et al.* 2008) is adopted for the modelling of the two square cylinders. The massively parallel solver 'Incompact3d' (Laizet & Lamballais 2009; Laizet, Lamballais & Vassilicos 2010; Laizet & Li 2011), which is based on a Cartesian mesh, is used to solve the incompressible

Case	Re_{T_0}	L_d/T_0	X_{bar}/T_0	L_X/T_0	L_Y/T_0	L_Z/T_0	N_X	N_Y	N_Z
WI4	2500	4	8	35	28	5	801	700	100
WI6	2500	6	8	35	30	5	801	690	100
WI8	2500	8	8	35	34	5	801	748	100

TABLE 1. Geometric and numerical details.
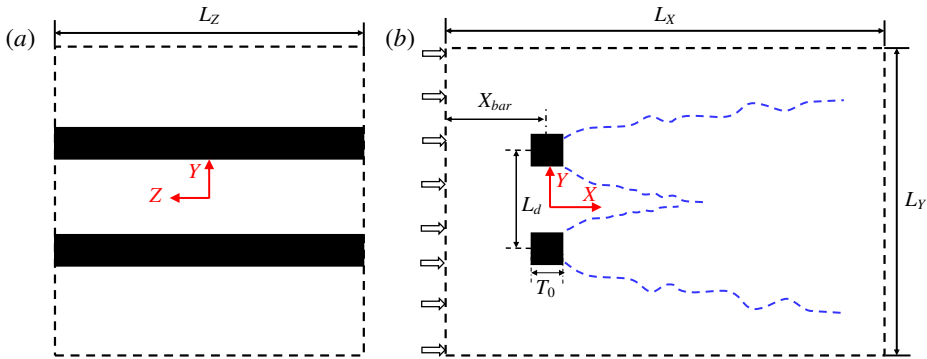
FIGURE 1. (Colour online) (*a*) Schematic front view and (*b*) schematic side view of the computational domain.

Navier–Stokes equations. The sixth-order central compact schemes proposed by Lele (1992) are used for the spatial discretion. Concerning the time advancement, the third-order Adams–Bashforth scheme is adopted with a time step $\Delta t = 0.0045 T_0/U_{in}$ and data are averaged over 200 000 time steps for all three cases. In the current DNS, the maximum Courant–Friedrichs–Levy number is 0.14. Refer to Laizet & Lamballais (2009), Laizet *et al.* (2010) and Laizet & Li (2011) for a detailed description of the DNS code and the corresponding parallel strategy.

Redford, Castro & Coleman (2012) demonstrated that to avoid significant contamination on the wake growth imposed by the boundary conditions, the smallest lateral domain size (L_Y in our current study) is $L_Y \simeq 5.9\delta$, where δ is the wake half-width. As shown in figure 2(*a*), the two wakes have not yet fully merged together even at the most downstream location for all three cases. Thus, we could not directly use this criterion in our current study. Instead, we propose a quasi-half-width b which is defined as the vertical distance from the centreline to the location where $(U - U_{min})/U_0 = 1/2$ with $U_0 = (U_c - U_{min})$ being the quasi-velocity deficit (see figure 2*b*). The ratios L_Y/b for the cases with $L_d/T_0 = 4$, 6 and 8 are 8.6, 6.7 and 5.9, respectively, at the furthest downstream location considered (i.e. $X/T_0 = 26$). Even for the case with the largest separation distance, the lateral domain size satisfies the criterion proposed by Redford *et al.* (2012) at the most downstream location. Therefore, the vertical size of our simulation domain is sufficiently large.

The spatial resolutions $(\Delta X \Delta Y \Delta Z)^{1/3}$ with respect to the Kolmogorov microscale η along the centreline are explored (not shown herein), where $\eta = (\nu^3/\varepsilon)^{1/4}$. Here, $\varepsilon = 2\nu\langle s_{ij}s_{ij}\rangle$ with the strain rate s_{ij} being $(\partial u_i'/\partial x_j + \partial u_j'/\partial x_i)/2$, where the angled brackets $\langle\rangle$ refer to an average over time t and Z. Laizet *et al.* (2015*a*) investigated the influence of the spatial resolution on the turbulent flow generated by a single square grid and demonstrated that a resolution of $\Delta \simeq 7\eta$ is fine enough to reproduce the
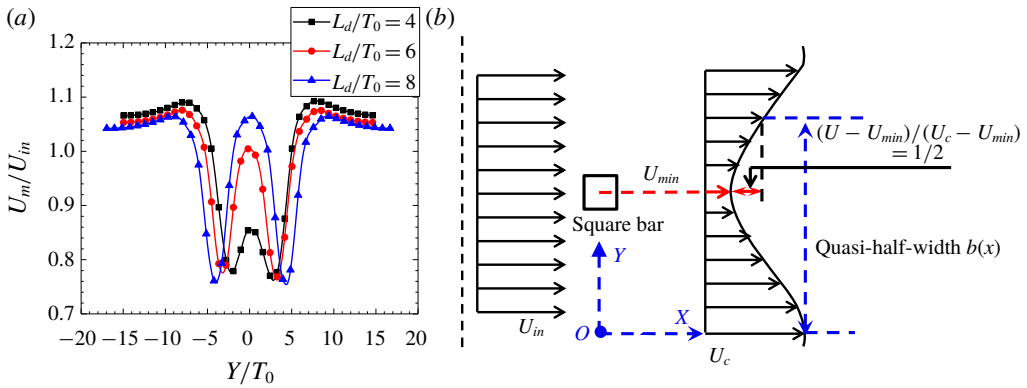
FIGURE 2. (Colour online) (*a*) Vertical distribution of U_m/U_{in} at a far downstream location (i.e. $X/T_0 = 26$) for all three cases. (*b*) Definition sketch of the quasi-half-width $b(x)$. The red dashed line presents the centreline of the square cylinder. The mean streamwise velocity U_{min} and velocity deficit $U - U_{min}$ are marked in red. Only the top half of the whole domain is shown.

first-, second-, third- and fourth-order momentums of one point velocities within an error of less than 10 %, whereas a higher resolution $\Delta \simeq 5\eta$ is enough to guarantee the numerical results of the first- and second-order momentums to within an error of 5 %. We confirmed the lowest spatial resolution is found in the case with $L_d/T_0 = 4$. Even for this case, the worst resolution is still below 5η. For the other two cases, the spatial resolution is always smaller than 3.4η. Therefore, the current mesh setting is fine enough to capture the turbulence behaviour. Further evaluations of numerical strategies and parameters are presented in supplementary appendices A, B and C; supplementary materials are available online at https://doi.org/10.1017/jfm.2019.456.

3. Wake interaction and extreme events

This work is devoted to the study of the extreme events and the energy spectra (also the second-order structure function) in turbulent flows behind two side-by-side square cylinders. Before delving deep into the relationship between the extreme events and the $-5/3$ spectra, in this section we explored some related fundamental aspects of dual-wake flows (e.g. wake-interaction pattern, wake-interaction length scale, spatial evolution of various turbulence characteristics and formation mechanisms of the extreme events), which represent actually the first important objective of this work.

3.1. *Flow visualizations*

In figure 3, the magnitudes of the normalized instantaneous vorticity $\Omega/(U_{in}/T_0)$, where $\Omega = (\Omega_i\Omega_i)^{1/2}$ with $\Omega_i = \varepsilon_{ijk}\partial u_k/\partial x_j$ and ε_{ijk} being the Levi-Civita symbol, are plotted for all three cases in the X–Y plane, which certainly provides insights into the wake-interaction patterns, at least to some extent. Figure 3 shows that perceptible oscillations can be found upstream of the cylinders. A similar spike-like behaviour was also reported in the DNSs of turbulent flow in Trias, Gorobets & Oliva (2015), although in their paper a contour plot of the Kolmogorov length scale η is presented. Obviously, the Kolmogorov length scale is closely related to the velocity gradients. Thus, the existence of the oscillations is related to the fact that streamlines can be distorted upstream of the cylinders.
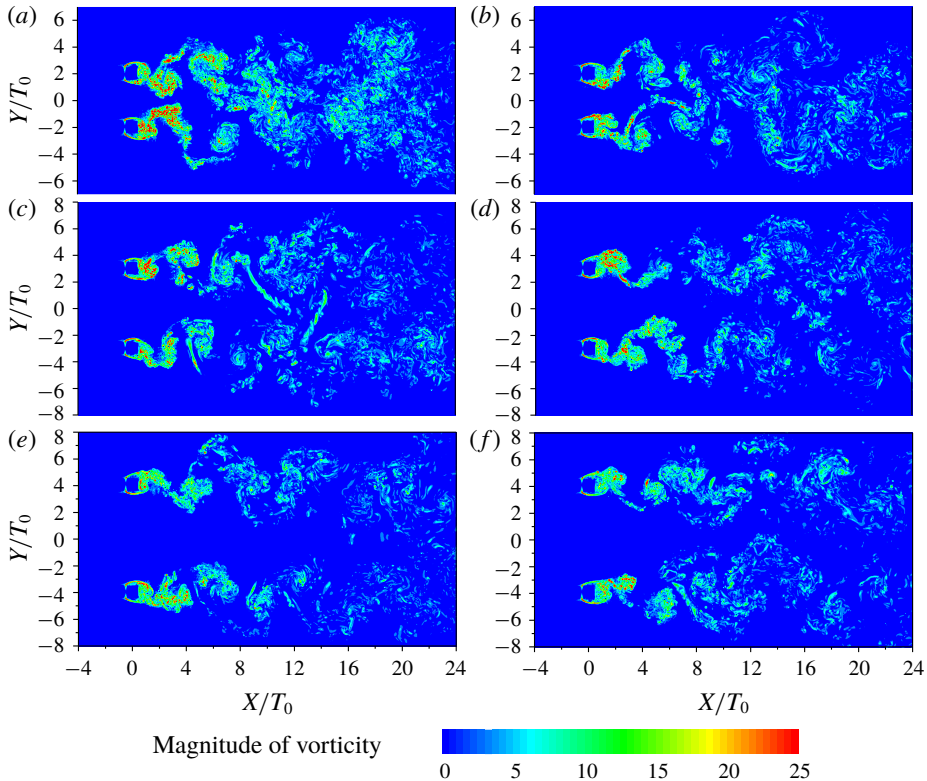
FIGURE 3. (Colour online) Visualizations of the magnitude of instantaneous vorticity $\Omega/(U_{in}/T_0)$ in the X–Y plane. (*a,b*) $L_d/T_0 = 4$; (*c,d*) $L_d/T_0 = 6$; (*e,f*) $L_d/T_0 = 8$. All maps cover only part of the simulation domain and are shown on a linear scale. Note that to visualize the wake-interaction pattern, for each of the cases considered two randomly selected instantaneous flow fields are plotted.

By and large, two different flow patterns can be observed depending on the separation distance between the cylinders. For the case with $L_d/T_0 = 4$, the gap flow is weak and beyond $X/T_0 = 8$ only one large wake can be observed. For the cases with large gap ratios ($L_d/T_0 = 6$ and 8), the gap flow is straight and the two vortex streets persist longer downstream. Thus, depending on the strength of the gap flow, the three simulation cases can be simply divided into two regimes: weak gap flow regime and robust gap flow regime. In the weak gap flow regime, two vortex streets merge into one, whilst in the robust gap flow regime with a large separation between the square cylinders, the two vortex streets do not merge. One could reasonably expect that the two vortex streets in the robust gap flow regime will finally merge in the further downstream region. However, in this study, owing to the limited streamwise length, the combination of the two wakes is not significant, as suggested by figure 2.

3.2. *Wake-interaction length scale*

In the preceding subsection, two different flow patterns can be identified. In this subsection, we shall demonstrate that the turbulence characteristics in different regimes are quite different based on the wake-interaction length scale. As suggested
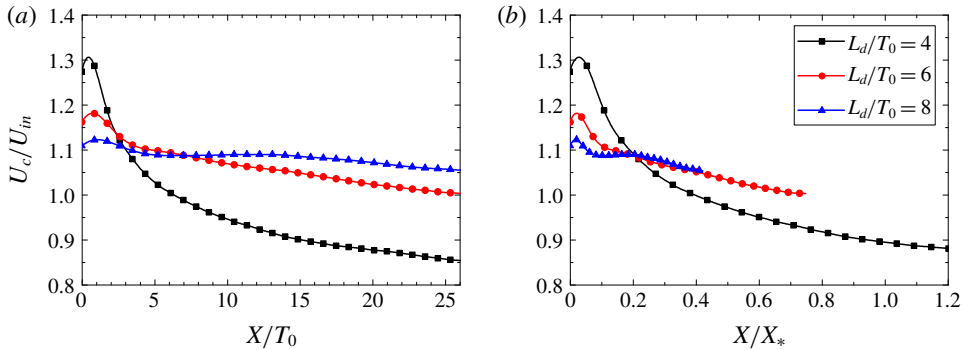
FIGURE 4. (Colour online) Streamwise evolution of the mean velocity U_c along the centreline. (*a*) As a function of X/T_0; (*b*) as a function of X/X_*.

by Townsend (1956), the growth of the width of a plane turbulent wake follows $\delta \propto \sqrt{T_0 X}$. It is tempting to study the wake interactions behind two side-by-side square cylinders by using this scaling law, as has been done by Mazellier & Vassilicos (2010). For a given separation distance L_d, the two wakes are expected to meet at a downstream streamwise location X_* where $\delta(X_*) \propto \sqrt{T_0 X}$. Consequently, we can now derive the wake-interaction length scale as $X_* = L_d^2/T_0$. The original formula for the wake-interaction scale by Mazellier & Vassilicos (2010) has been improved by Gomes-Fernandes *et al.* (2012) to assess the drag coefficient of the wake generators.

The wake-interaction length scale X_* indeed has been successfully applied to fractal-generated turbulence (see, for example, Mazellier & Vassilicos 2010; Gomes-Fernandes *et al.* 2012; Nagata *et al.* 2013). In fractal-generated turbulence, the interactions of four wakes are involved, which significantly increase the complexities. Recall that the wake-interaction length scale is based on the interactions of two wakes. To fully investigate the wake interactions with different gap ratios L_d/T_0 and assess whether the evolution of turbulent flow scales with the wake-interaction length scale, various centreline statistics are considered.

In figure 4, we plot the streamwise evolution of the mean centreline velocity U_c/U_{in} versus X/T_0 (*a*) and X/X_* (*b*). Note that in previous studies concerning wake interactions (Zhou *et al.* 2001; Alam *et al.* 2011; Alam & Zhou 2013; Alam *et al.* 2016; Zheng & Alam 2017), the size of the square cylinder, i.e. T_0, was extensively used as a scaling parameter for no particular reason. Thus, in this work, in addition to the wake-interaction length scale X_*, the streamwise distance is also normalized by T_0. As one might expect, the value of U_c at $X/T_0 = 0$ decreases with the increase of the separation distance L_d/T_0. However, at $X/T_0 = 26$, which is the most downstream location considered, U_c/U_{in} in the case with $L_d/T_0 = 8$ becomes largest. When the streamwise distance X is normalized by X_*, the two profiles corresponding to the cases with $L_d/T_0 = 6$ and 8 collapse onto a single curve at $X/X_* > 0.2$. Thus, the largest U_c found in the case with $L_d/T_0 = 8$ at $X/T_0 = 26$ is attributed to its slower spatial evolution with respect to the coordinate distance X. It is not surprising that the wake-interaction length scale cannot be applied to the case with $L_d/T_0 = 4$, since only one large vortex street can be identified in the downstream region, as shown in figure 3. The evolution of the streamwise root mean square (r.m.s.) velocity U_{rms} along the centreline is given in figure 5. It is clear that the profile of the case with $L_d/T_0 = 4$ is fundamentally different from the other two profiles. However, due to the
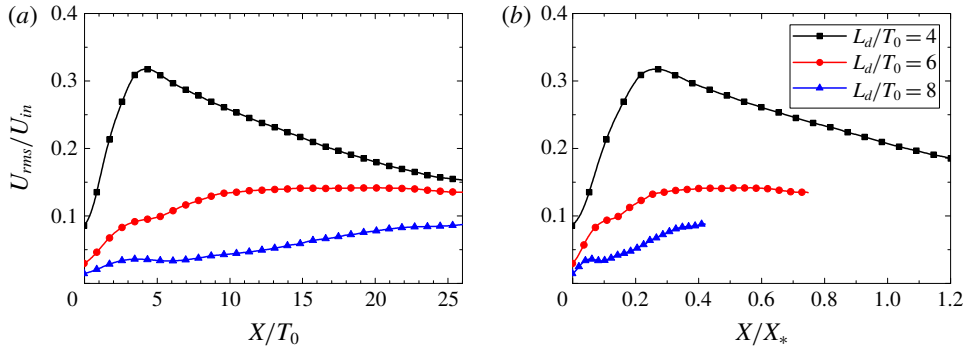
FIGURE 5. (Colour online) Streamwise evolution of the r.m.s. velocity U_{rms} along the centreline. (*a*) As a function of X/T_0; (*b*) as a function of X/X_*.

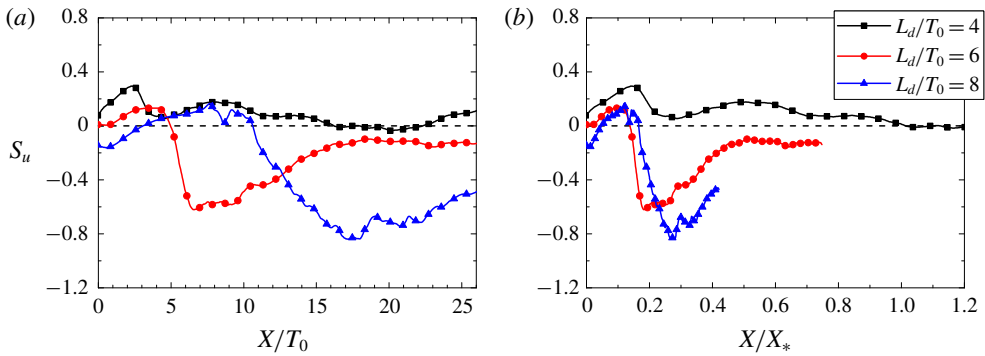

FIGURE 6. (Colour online) Streamwise evolution of the skewness of fluctuating streamwise velocity S_u along the centreline. (*a*) As a function of X/T_0; (*b*) as a function of X/X_*. The horizontal dashed line indicates $S_u = 0$.

limited streamwise length, the decay region is missing for the case with $L_d/T_0 = 8$. Thus, we could not draw a solid conclusion concerning the wake-interaction scale.

Figures 6 and 7 show the evolution of the centreline skewness S_u and flatness F_u, where $S_u = \langle u'^3 \rangle / \langle u'^2 \rangle^{3/2}$ and $F_u = \langle u'^4 \rangle / \langle u'^2 \rangle^2$. Extreme events with negative S_u and large F_u can only be found in the cases with larger gap ratios ($L_d/T_0 = 6$ and 8). In contrast, the profiles of S_u and F_u for the case with $L_d/T_0 = 4$ are more or less flat. The most intense events occur at $X/X_* \simeq 0.2$ and with downstream distance, S_u and F_u gradually acquire the corresponding values of a Gaussian distribution. Note that the location with the largest negative value of S_u, i.e. $X/X_* \simeq 0.2$, is close to the corresponding location in the turbulence generated by a single square grid (Zhou *et al.* 2014*a*; Laizet *et al.* 2015*b*). It is worth mentioning that in a previous study of the turbulence generated by a single square grid (Zhou *et al.* 2014*a*), the corresponding gap ratio was 9.1, which is close to the cases with $L_d/T_0 = 8$. It is therefore clear from figure 6 that only for the cases with larger L_d, can the extreme events be found and the distribution of the velocity fluctuations in the upstream region is highly non-Gaussian. As shown in figures 6 and 7, for the case with larger gap ratios ($L_d/T_0 = 6$ and 8) the use of the wake-interaction length scale X_* does return a better description
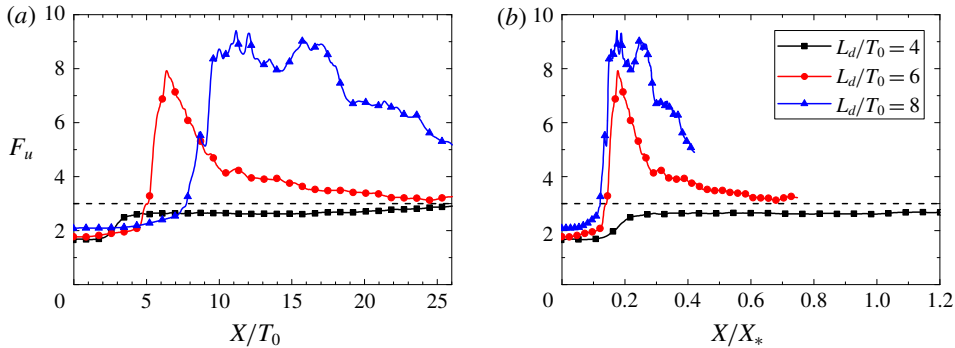
FIGURE 7. (Colour online) Streamwise evolution of the flatness of fluctuating streamwise velocity F_u along the centreline. (*a*) As a function of X/T_0; (*b*) as a function of X/X_*. The horizontal dashed line indicates $F_u = 3$.

of the streamwise evolution of S_u and F_u, albeit that the two profiles do not completely collapse and the profiles for the case with $L_d/T_0 = 8$ are not well converged.

In this subsection, we test the wake-interaction length scale X_* and reveal that for the case with $L_d/T_0 = 4$, the streamwise evolution of various centreline statistics does not scale with X_*. Recall that the derivation of X_* is based on the interactions of two independent wakes. And it is demonstrated that for the case with $L_d/T_0 = 4$ the two wakes merge into one in the downstream region (i.e. $X/T_0 > 8$). As a result, it is not surprising that the wake-interaction length scale cannot be applied. However, for the case with larger separation distance (i.e. $L_d/T_0 = 6$ and 8), some of the turbulence characteristics more or less scale with X_*, as happens in the case of the grid-generated turbulence, rather than simply X/T_0. Note that for a typical low-blockage space-filling grid, the corresponding L_d/T_0 is much larger. For example, as shown in Nagata *et al.* (2013) the ratios of the largest mesh size to the thickness of the largest bars considered are 12.4, 13.8 and 14.0, respectively. Thus, the separation distances considered (i.e. $L_d/T_0 = 4$, 6 and 8) may not well represent the two wake problem when the wakes are far enough from each other.

3.3. *Extreme events*

As mentioned in the introduction, extreme events can be closely related to the appearance of the $-5/3$ spectra. In this subsection, the characteristics along with the formation mechanism of the extreme events shall be discussed. It can be seen that extreme events are found in the cases with relatively larger gap ratios, namely, $L_d/T_0 = 6$ and 8. For the case with the largest gap ratio $L_d/T_0 = 8$, however, the dual-wake flow still undergoes transition at the furthest downstream location at which the numerical data are available and the corresponding skewness S_u takes a large negative value. From now on we therefore concentrate attention on the case with $L_d/T_0 = 6$, which allows us to perform a complete investigation of the extreme events.

Figure 8 shows the PDFs of the streamwise velocity fluctuations u' and their time derivative $\partial u'/\partial t$ at $X/T_0 = 6$ and 26. Note that at $X/T_0 = 6$ the most intense events occur, whereas the turbulent flow is almost Gaussian distributed at $X/T_0 = 26$ (i.e. $S_u \simeq 0$ and $F_u \simeq 3$). The distributions of u' and $\partial u'/\partial t$ at $X/T_0 = 6$ have significant fat tails
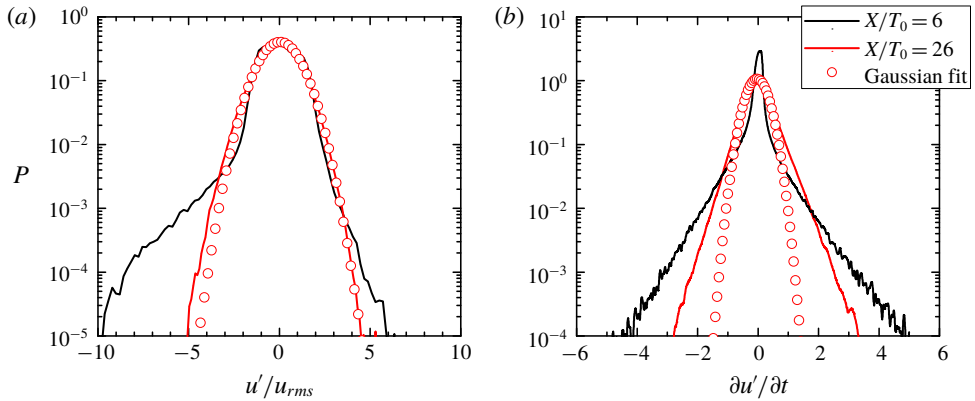
FIGURE 8. (Colour online) PDF distributions of (*a*) u' and (*b*) $\partial u'/\partial t$ at $X/T_0 = 6$ and 26. The corresponding Gaussian fits at $X/T_0 = 26$ (represented by red open circles) are also plotted for comparison.
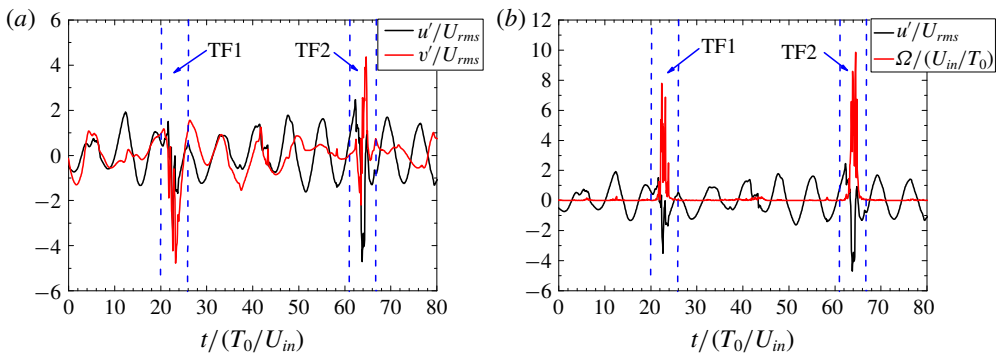

FIGURE 9. (Colour online) Time traces of (*a*) u'/U_{rms} and v'/V_{rms} and (*b*) time traces of Ω and u'/U_{rms} at $X/T_0 = 6$ and $Y/T_0 = 0$. The origin of time for all lines is the same. Two different time frames (TF1 and TF2) with the appearance of extreme events can be identified.

compared with those at $X/T_0 = 26$, suggesting the probability of the rare events (i.e. intense value of u' and $\partial u'/\partial t$) at $X/T_0 = 6$ is considerably larger.

To provide deeper insight into the extreme events, figure 9(*a*) presents the time traces of the centreline velocity fluctuation u'/U_{rms} and v'/V_{rms} at $X/T_0 = 6$, where v' and V_{rms} are the vertical velocity fluctuations and the corresponding r.m.s. velocity, respectively. The variations of u' and v' are relatively smooth and exhibit quasi-periodic (regular) oscillations except for the TF1 and TF2. Figure 9(*b*) shows the time evolution of the magnitude of vorticity Ω and u' at $X/T_0 = 6$, which suggests that non-turbulent regions (i.e. quiescent regions with negligibly small magnitude of vorticity) are dominant. The occurrences of the extreme events are only found in the turbulent region (i.e. fluctuating region with high vorticity). Note that in the case of the dual-wake flow, the most intense events occur at a location where the flow is not always in the turbulent region, as in the turbulence generated by a single square grid
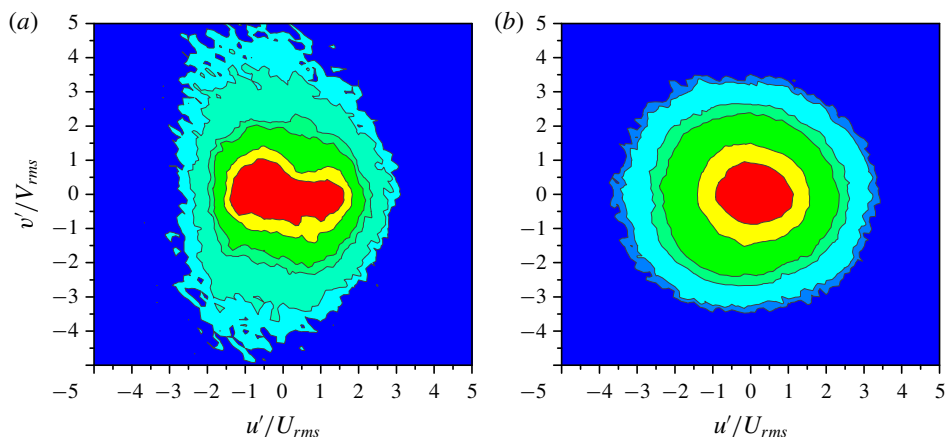
FIGURE 10. (Colour online) Joint PDFs of u'/U_{rms} and v'/V_{rms}. (a) At $X/T_0 = 6$; (b) at $X/T_0 = 26$. A total of six contour levels (i.e. 0.1, 0.05, 0.01, 0.005, 0.001 and 0.0005) are shown.

(see figures 5 and 8 in Zhou *et al.* (2014a); figures 9 and 10 in Laizet *et al.* (2015b)). Another finding from figure 9 concerning the occurrence of the extreme events is that u' and v' are closely correlated (i.e. in phase within TF1 and anti-phased within TF2). More quantitatively, the joint PDFs of u' and v' at $X/T_0 = 6$ are shown in figure 10. The joint PDFs at a further downstream location $X/T_0 = 26$ are also presented for comparison. Figure 10(a) suggests that the flow particles with either high positive or high negative v' tend to possess large negative u'. This observation is therefore in accord with the assumption that the large magnitude of v' is more likely to be associated with a large negative u'. The contour lines corresponding to rare events are approximately symmetrical with respect to the horizontal line, i.e. $v'/V_{rms} = 0$, confirming that u' and v' can be either in phase or out of phase with each other. At $X/T_0 = 26$, however, all contour lines acquire a 'pancake' shape instead, suggesting that u' and v' are essentially statistically uncorrelated.

The formation of the extreme events can be explained by using a Lagrangian description. One can imagine that the local fluid particles along the centreline with large magnitude of v' have a better chance of being from a location with a larger vertical distance from the centreline. In the near field of a square cylinder, the turbulent wake consists of vortex tube clusters, which are usually characterized by a large magnitude of vorticity, and the velocity deficit is still significant. These slower vortex tube clusters serve as obstacles and can easily slow down the local turbulent flow, resulting in the extreme events with negative S_u. Relying on the direction of the vertical movement, u' and v' can be either in phase or out of phase with each other along the centreline as shown in figures 9 and 10.

4. Energy spectra and structure functions

In this section, we shall answer the two important remaining questions: the relationship between the occurrence of the extreme events and the well-defined $-5/3$ energy spectra and also the characteristics of the second-order structure function at the location where the extreme events occur and the flow is highly intermittent.
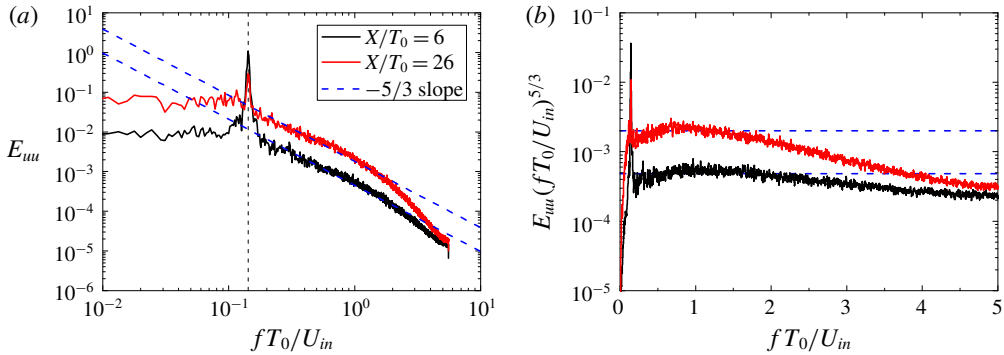
FIGURE 11. (Colour online) (*a*) Energy spectra of u' at $X/T_0 = 6$ and 26 for the case with $L_d/T_0 = 6$. The vertical dashed line indicates $St = fT_0/U_{in} = 0.142$; (*b*) the corresponding compensated energy spectra $E_{uu}(fT_0/U_{in})^{5/3}$. The horizontal (i.e. frequency) axis is linear.

4.1. *One-dimensional energy spectra*

Before investigating the relationship between the extreme events and the energy spectra, we need to obtain the shape of the one-dimensional energy spectra first. The one-dimensional energy spectra of the streamwise velocity fluctuation u' at $X/T_0 = 6$ and 26 along the centreline for the case with $L_d/T_0 = 6$ are given in figure 11. Note that at the upstream location (i.e. $X/T_0 = 6$) the turbulent flows are highly non-Gaussian distributed and highly intermittent, whereas at the far downstream location (i.e. $X/T_0 = 26$) the flow field becomes approximately Gaussian distributed and approximately fully turbulent. The spectra at the two chosen locations display pronounced peaks at the normalized frequency $St = fT_0/U_{in} = 0.142$ corresponding to the vortex shedding frequency (more specifically, the regular and slow oscillation of u' at $X/T_0 = 6$ as shown in figure 9). The dominant frequency $fT_0/U_{in} = 0.142$ is approximately half the value found in the flow behind a single square cylinder. For example, as presented in Portela, Papadakis & Vassilicos (2017) when the inlet Reynolds number is $Re_{T_0} = 3900$, the corresponding fT_0/U_{in} is 0.267. In a previous experiment of dual-wake flows with a slightly smaller gap ratio $L_d/T_0 = 5$ and much larger inlet Reynolds number $Re_{T_0} = 47\,000$, the returned St is 0.128, which is close to our simulation result (Alam & Zhou 2013).

Compared with $X/T_0 = 26$, at $X/T_0 = 6$ the vortex shedding contains more energy; that is the peak value of E_{uu} is much larger at $X/T_0 = 6$. However, except for the narrow frequency range corresponding to vortex shedding, the energy spectrum at $X/T_0 = 6$ is always much smaller than that at $X/T_0 = 26$. This is due to the smooth evolution of u' as shown in figure 9, albeit the extreme events bearing large fluctuating energy (see figure 9). Note that even the velocity fluctuations at $X/T_0 = 6$ and 26 appear to have more or less identical strengths (magnitudes of U_{rms}) (see figure 5), their intrinsic properties are actually quite different as already shown in figures 8 and 11.

The energy spectrum at $X/T_0 = 6$ exhibits a well-defined $-5/3$ power law with a range for more than a decade. With downstream distance, however, the range of the $-5/3$ power law is eroded, albeit the corresponding r.m.s. velocity is even slightly larger (see figure 5) and the local Reynolds numbers based on the Taylor microscale remains approximately unchanged, that is, $Re_\lambda \simeq 100$ (not shown herein). Another

interesting finding is that for both locations, the shedding frequency $St = 0.142$ defines the beginning of the $-5/3$ power-law energy spectra.

Similar observations have already been reported in various kinds of turbulent flows. For instance, in the near field of grid-generated turbulence (single square grid (Laizet *et al.* 2015*b*; Paul *et al.* 2017), regular grid (Isaza, Salazar & Warhaft 2014), fractal grid (Laizet, Vassilicos & Cambon 2013; Hearst & Lavoie 2014)), the power spectrum exhibits a well-defined power law with an exponent close to $-5/3$ and the range of the $-5/3$ scaling narrows with downstream distance. Zhou *et al.* (2018) demonstrated in a dual-plane jet flow, the range of the $-5/3$ power law also decreases further downstream. Even downstream of a single square prism, a similar observation can also be found (Portela *et al.* 2017).

4.2. *Filtered fluctuating velocity fields*

To take the observation in the preceding subsection (i.e. well-defined $-5/3$ spectra can be found at both streamwise locations considered) one step further, the relationship between the energy spectra and the extreme events will be discussed here. At $X/T_0 = 6$, the flow field is not fully turbulent; there are alternations between laminar large-scale oscillations and strong turbulent fluctuations (e.g. TF1 and TF2). To shed light on the physical mechanism responsible for the wider range of the $-5/3$ power law at $X/T_0 = 6$ in the high-frequency range, we first attempt to subtract the signal in the low-frequency range. The velocity fluctuating signals are passed through a highpass filter with the low cutoff frequency fT_0/U_{in} being 2.0. Thus, the filter data are expected to contain signals with frequency fT_0/U_{in} larger than 2.0, where the $-5/3$ power law is absent. Throughout this paper, the velocity data are filtered using eighth-order zero-lag (i.e. bidirectional) Butterworth filters (e.g. highpass, bandpass and lowpass filters). And the scripts $<$, $\sim$ and $>$ stand for statistics associated with high-, intermediate- and low-frequency components, respectively. For instance, the velocity fluctuation can be decomposed as $u' = u'_> + u'_\sim + u'_<$. The use of high-order filters allows us to efficiently remove the unwanted components. Considering the fact that filters chosen are bidirectional, the filtered signals can be expected to be delay compensated. A further validation of the involved filtering processes is given in supplementary appendix D.

Figure 12(*a*) shows the spectrum of filtered velocity fluctuations $u'_<$ corresponding to the high-frequency range $fT_0/U_{in} > 2.0$. For comparison, the spectrum of the entire fluctuating signal u' already shown in figure 11 is also included. The profile corresponding to $u'_<$ in the high-frequency range remains virtually intact and unaffected. In contrast, the fluctuating signals within the low-frequency range are efficiently subtracted. We now apply the chosen highpass filter to the time traces of u' shown in figure 9. As can be seen in figure 12(*b*), except for the fluctuating signals in the TF1 and TF2, the filtered signals are in a relatively quiescent state with negligible magnitude. This observation suggests that the high-frequency signals contribute to the extreme events.

We further divide the intermediate range (i.e. $0.2 < fT_0/U_{in} < 2.0$), where the $-5/3$ spectrum can be found, into two subranges ($u'_\sim = u'_{\sim,l} + u'_{\sim,h}$) to explore the erosion of the $-5/3$ scaling. Figures 13(*a*) and 13(*b*) show the energy spectrum and the velocity signal in the high-frequency zone of the $-5/3$ scaling range (i.e. $0.8 < fT_0/U_{in} < 2.0$). The fact that the non-zero fluctuations are mainly found in TF1 and TF2 indicates an intimate relationship between intermittent events and the extended $-5/3$ power law. In other words, we could safely draw the conclusion that the occurrences of the
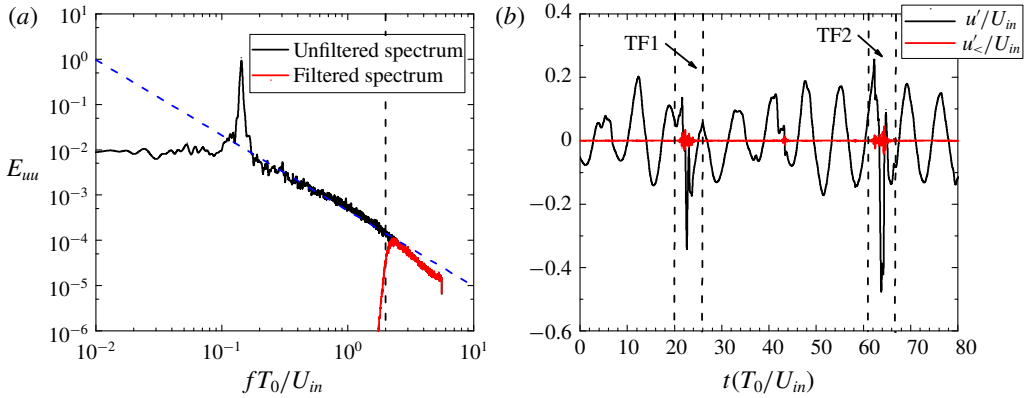
FIGURE 12. (Colour online) (*a*) Energy spectrum of the filtered velocity signal $u'_</U_{in}$ subject to a highpass filter with a cutoff frequency of 2.0. Energy spectrum of the original velocity signal (i.e. entire signal) u' is also shown for comparison. The vertical dashed line indicates $fT_0/U_{in} = 2$. (*b*) Time traces of the filtered signals $u'_</U_{in}$. The time evolution of the original velocity signals u' shown in figure 9 is also plotted as a comparison.
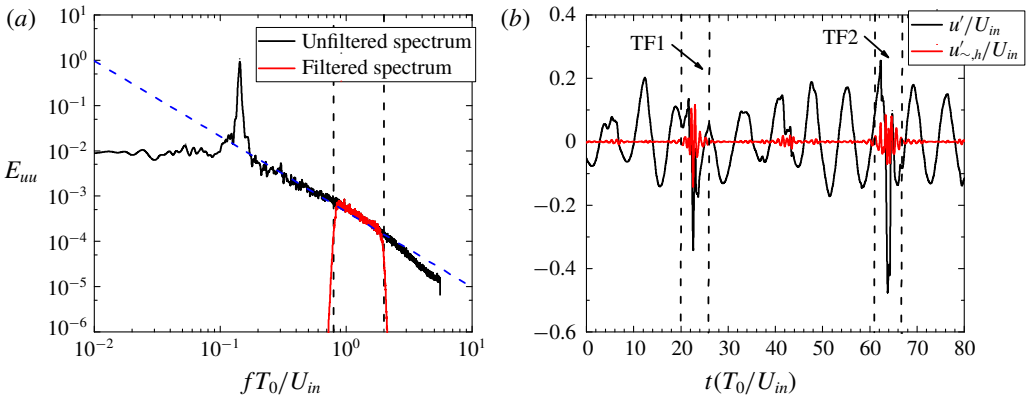

FIGURE 13. (Colour online) (*a*) Energy spectrum of the filtered velocity signal $u'_{\sim,h}/U_{in}$ subject to a band-pass filter with a lower cutoff frequency of 0.8 and a higher cutoff frequency of 2.0. Energy spectrum of the original velocity signal (i.e. entire signal) u' is also shown for comparison. The vertical dashed lines indicate $fT_0/U_{in} = 0.8$ and 2.0. (*b*) Time traces of the filtered signal $u'_{\sim,h}/U_{in}$. The time evolution of the original velocity signal u' shown in figure 9 is also plotted as a comparison.

extreme events (TF1 and TF2) contribute to the formation of the $-5/3$ power law in the high-frequency range (i.e. $fT_0/U_{in} \gtrsim 0.8$ in figure 12*b*). The range over which the $-5/3$ power law can be found therefore is determined by two turbulence behaviours, one being the large-scale vortex shedding and the other being the occurrence of the extreme events. With increasing downstream distance, the strength of the extreme events becomes weaker (see figure 6*a*), which results in the deterioration of the range of the $-5/3$ power law.
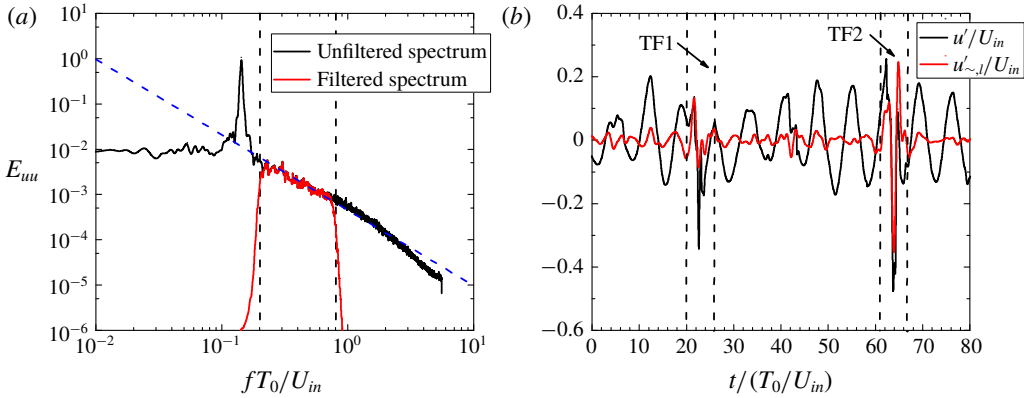
FIGURE 14. (Colour online) (*a*) Energy spectrum of the filtered velocity signal $u'_{\sim,l}/U_{in}$ subject to a band-pass filter with a lower cutoff frequency of 0.2 and a higher cutoff frequency of 0.8. Energy spectrum of the original velocity signal (i.e. entire signal) u' is also shown for comparison. The vertical dashed lines indicate $fT_0/U_{in} = 0.2$ and 0.8. (*b*) Time traces of the filtered signal $u'_{\sim,l}/U_{in}$. The time evolution of the original velocity signal u' shown in figure 9 is also plotted as a comparison.

It must, however, be pointed out that there is a large part of the −5/3 power law which is not in the highpass filtered field, that is, the intermediate-frequency range $0.2 \lesssim t/(T_0/U_{in}) \lesssim 0.8$. To investigate what is responsible for this part of the spectrum, we use a bandpass filter to extract the velocity signals within this range. And the higher and lower cutoff frequencies are set to $fT_0/U_{in} = 0.8$ and 0.2, respectively (see figures 14*a* and 14*b*). The time-traces of the filtered signals $u'_{\sim}$ demonstrate that the strength of the filtered velocity $u'_{\sim}$ is weak and as expected the oscillation behaviour possesses smaller periods. In contrast to the formation of the −5/3 scaling in the high-frequency range where the turbulent motions are dominant, in the intermediate-frequency range both laminar and turbulent motions contribute to the appearance of the −5/3 scaling.

Let us finally consider the behaviour in the low-frequency range (i.e. $fT_0/U_{in} \lesssim 0.2$), which stems from large-scale vortex shedding. A lowpass filter with the cutoff frequency of $fT_0/U_{in} = 0.2$ is used. Expect for TF1 and TF2, as shown in figure 15(*b*) the large-scale periodic oscillations of $u'_{>}$ corresponding to the energy containing range hold most of the energy.

Figure 16 shows the PDFs of the normalized velocity components $u'_{>}/U^{>}_{rms}$, $u'_{\sim}/U^{\sim}_{rms}$ and $u'_{<}/U^{<}_{rms}$ at $X/T_0 = 6$. The probability distribution of u'/U_{rms} is shown for comparison. Except for the profile corresponding to $u'_{<}$, all other probability distributions are negatively skewed and the profiles of $u'_{\sim}$ and $u'_{<}$ exhibit pronounced fatter tails. The statistical characteristics of u', $u'_{>}$, $u'_{\sim}$ and $u'_{<}$ (e.g. r.m.s., skewness and flatness) at $X/T_0 = 6$ and 26 are listed in table 2. For instance, the skewness of $u'_{>}$ is obtained as $S(u'_{>}) = \langle u'^3_{>} \rangle / \langle u'^2_{>} \rangle^{3/2}$. At the downstream location $X/T_0 = 26$, the definitions of the components $u'_{>}$, $u'_{\sim}$ and $u'_{<}$ are the same as those at $X/T_0 = 6$. The negative values of $S(u'_{>})$ and $S(u'_{\sim})$ at $X/T_0 = 6$ imply that the probability distributions within different frequency ranges are negatively skewed, whereas $S(u'_{<}) \simeq 0$ suggests a symmetrical shape. And the velocity signals in the intermediate- and high-frequency ranges are significantly intermittent for $F(u'_{\sim}) = 33$ and $F(u'_{<}) = 79$. These findings
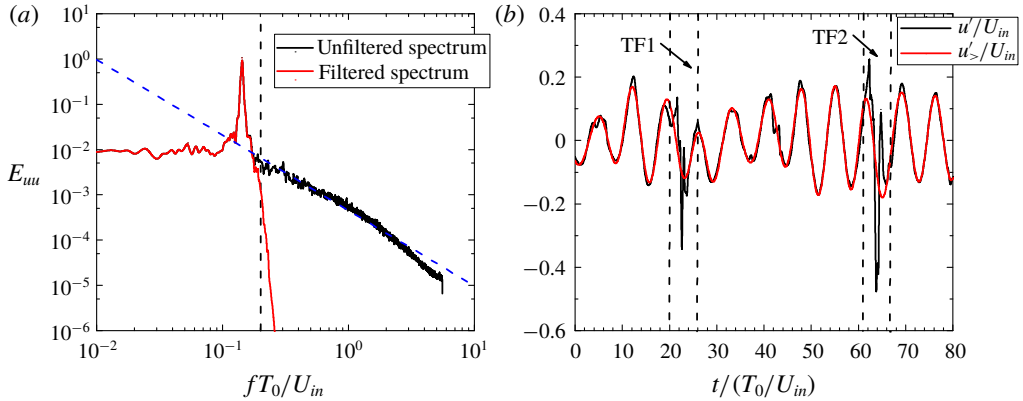
FIGURE 15. (Colour online) (*a*) Energy spectrum of the filtered velocity signal $u'_>/U_{in}$ subject to a lowpass filter with a lower cutoff frequency of 0.2. Energy spectrum of the original velocity signal (i.e. entire signal) u' is also shown for comparison. The vertical dashed line indicates $fT_0/U_{in} = 0.2$. (*b*) Time traces of the filtered signal $u'_>/U_{in}$. The time evolution of the original velocity signal u' shown in figure 9 is also plotted as a comparison.

X/T_0	U_{rms}	$U^>_{rms}$	$U^\sim_{rms}$	$U^<_{rms}$	$S(u')$	$S(u'_>)$	$S(u'_\sim)$	$S(u'_<)$	$F(u')$	$F(u'_>)$	$F(u'_\sim)$	$F(u'_<)$
6	0.11	0.098	0.038	0.012	−0.47	−0.21	−1.5	0.0087	6.8	3.0	33	79
26	0.14	0.11	0.077	0.018	−0.13	−0.16	−0.033	0.028	3.2	3.1	3.7	6.8

TABLE 2. Strength (i.e. r.m.s.), skewness and flatness of u', $u'_>$, $u'_\sim$ and $u'_<$ at $X/T_0 = 6$ and 26.

are in accord with the corresponding probability distributions shown in figure 16. With downstream distance at $X/T_0 = 26$, the magnitudes of the flatness are close to that of a Gaussian distribution.

The intermittent features found at $X/T_0 = 6$ in the intermediate- and low-frequency ranges are distinctly different from the so-called 'dissipation-range intermittency', which is believed to be only associated with scales that are comparable to or smaller than the Kolmogorov dissipation scale (see, for example, Frisch (1995) and references therein). It has been suggested that the concept of 'dissipation-range intermittency' does not necessarily violate the self-similarity in the inertial subrange, which is not the case for our study.

We close this subsection with a short remark concerning the appearance of a well-defined $-5/3$ power-law spectrum in the near field, where the turbulent flow is still developing and suffers a subsequent deterioration in the $-5/3$ range. First, the corresponding velocity fluctuations are highly intermittent, which can be roughly resolved into two parts, one being the large-scale vortex shedding and the other being the occurrence of the extreme events. As has already been confirmed in § 3, the formation of the extreme events is not necessarily directly related to the local Reynolds number. This suggestion is in accord with the previous findings that a well-defined $-5/3$ power law can be found at the location where the local Reynolds number is very small. Similar conclusions have been drawn by previous researchers.
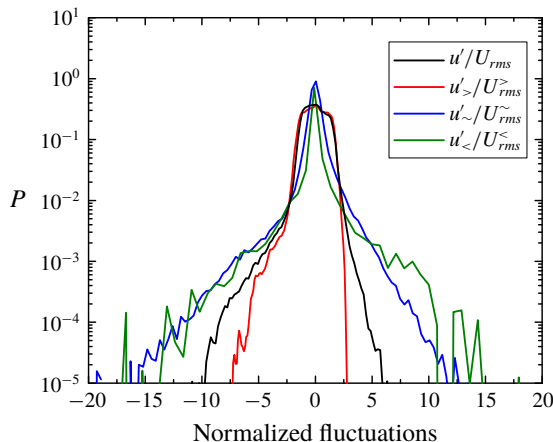
FIGURE 16. (Colour online) Probability distributions of $u'_>/U^>_{rms}$, $u'_\sim/U^\sim_{rms}$ and $u'_</U^<_{rms}$ at $X/T_0 = 6$. The profile of $P(u'/U_{rms})$ is also shown for comparison.

It was pointed out by Kraichnan (1974) that 'Kolmogorov's 1941 theory has achieved an embarrassment of success. The $-5/3$-spectrum has been found not only where it reasonably could be expected but also at Reynolds numbers too small for a distinct inertial range to exist and in boundary layers and shear flows...'. A similar but more recent statement is as follows: 'Conditions for the occurrence of a $-5/3$ spectrum appear to be more "forgiving" than those initially outlined by Kolmogorov' (Isaza *et al.* 2014).

It is the large-scale vortex shedding and the occurrence of the intermittent fluctuations instead of the local Reynolds number Re_λ that actually determine the range of the $-5/3$ power law. Our current work contributes to the understanding of the appearance of the $-5/3$ power-law scaling in the near field of a spatially developing turbulent flow (see, for example, Gomes-Fernandes *et al.* 2014; Laizet *et al.* 2015b; Paul *et al.* 2017; Portela *et al.* 2017). Finally, it should be stressed that the frequency range over which the spectrum has an exponent close to $-5/3$ is defined by two distinctly different behaviours corresponding to large-scale vortex shedding and occurrence of the extreme events. This finding obviously disobeys the predictions given by Kolmogorov (1941a,b,c). It must be pointed out that in this work, we confirm that the extreme events and the $-5/3$ energy spectrum at $X/T_0 = 6$ are closely related. One cannot claim that it is the extreme events that are causing the $-5/3$ energy spectrum.

4.3. *Second-order structure function*

In this subsection, we address the final question raised in the introduction section, that is, the shape of the second-order structure function in the flow region where the extreme events can be identified. Thus, we explore the second-order structure function $\langle \delta u'^2(\Delta t) \rangle$ with $\delta u'(\Delta t)$ being $u'(t + \Delta t) - u'(t)$ at the two extensively investigated locations (i.e. $X/T_0 = 6$ and 26). According to our definition, the second-order structure function $\langle \delta u'^2(\Delta t) \rangle$ depends on the streamwise location X and time difference Δt. According to the Kolmogorov phenomenology, in the so-called 'inertial subrange' we have the well-known $2/3$ power law (i.e. equivalent to the $-5/3$ energy spectrum
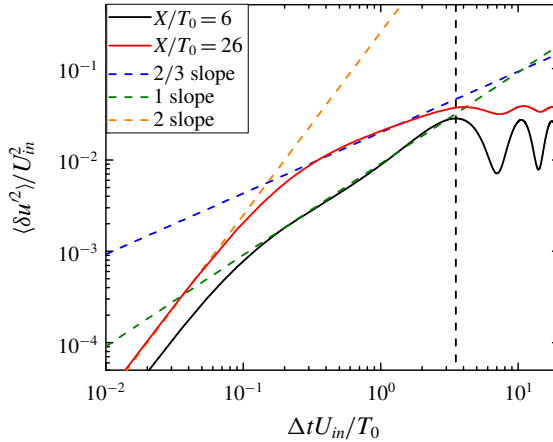
FIGURE 17. (Colour online) Second-order structure functions $\langle \delta u'^2(\Delta t) \rangle$ at $X/T_0 = 6$ and 26 along the centreline. The vertical dashed line corresponds to half-vortex shedding cycle (i.e. the phase difference between $u'(\Delta t)$ and $u'(t + \Delta t)$ is π).

in frequency space) albeit the range of the 2/3 power law in real space is always much smaller than the frequency range over which the $-5/3$ power law can be found (see, for example, Tennekes & Lumley 1972; Frisch 1995; Pope 2000). It is worth mentioning that structure functions considered here are actually averaged structure functions.

Figure 17 shows $\langle \delta u'^2(\Delta t) \rangle$ versus $\Delta t U_{in}/T_0$ at $X/T_0 = 6$ and 26 along the centreline. At $X/T_0 = 6$ the expected 2/3 power law is absent and the turbulent flow exhibits a substantial power-law range with a large exponent close to 1 in the intermediate range $0.1 \lesssim \Delta t U_{in}/T_0 \lesssim 3$ instead. In contrast, at the downstream location $X/T_0 = 26$ the second-order structure function acquires an approximate 2/3 scaling law within the intermediate range $0.3 \lesssim \Delta t U_{in}/T_0 \lesssim 3$, which is in accord with Kolmogorov's prediction. Compared with the upstream location $X/T_0 = 6$, at $X/T_0 = 26$ the $-5/3$ frequency range is smaller but still a discernible 2/3 power law can be identified. Thus, the absence of the 2/3 scaling law at $X/T_0 = 6$ is unlikely to be associated with the squeezing effect introduced by the Fourier transform.

For sufficiently small Δt, the Taylor expansion of the velocity difference is $u'(t + \Delta t) - u'(t) = (\partial u'(t)/\partial t)\Delta t + O(\Delta t^2)$. The second-order structure is therefore $\langle \delta u'^2(\Delta t) \rangle = \langle (\partial u'(t)/\partial t)^2 \rangle \Delta t^2 + O(\Delta t^3)$. Figure 17 further shows that for small Δt, the second-order structure functions at $X/T_0 = 6$ and 26 indeed acquire a well-defined power law with an exponent close to 2, implying that in current DNSs the small dissipation scales are well resolved in time.

To shed light on the formation mechanism of the substantial 1 power law at $X/T_0 = 6$, the second-order structure functions of the filtered flow fields (i.e. $u'_>$, $u'_\sim$ and $u'_<$) are computed (see figure 18a). The second-order structure functions at $X/T_0 = 26$ are shown in figure 18(b) as a further comparison. Obviously, at sufficiently large Δt, we have $\langle \delta u'^2_<(\Delta t) \rangle = 2(U^<_{rms})^2$, $\langle \delta u'^2_\sim(\Delta t) \rangle = 2(U^\sim_{rms})^2$ and $\langle \delta u'^2_>(\Delta t) \rangle = 2(U^>_{rms})^2$, which is indeed the case as shown in both figures 18(a) and 18(b).

From Parseval's theorem, we can derive the following relations:

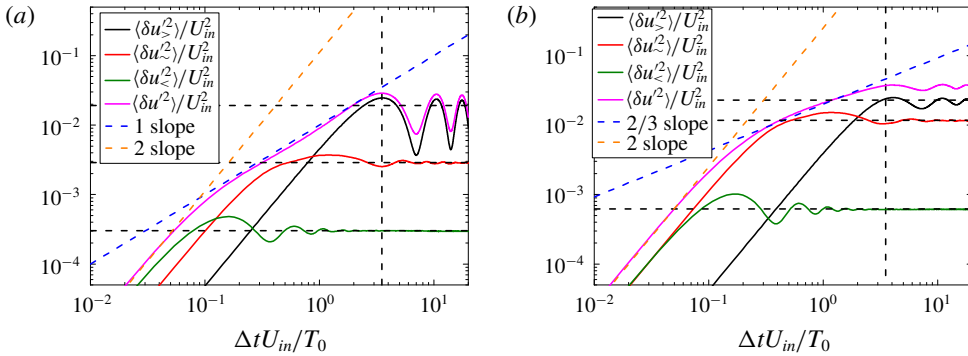$$\langle \delta u'^2(\Delta t) \rangle = \langle \delta u'^2_<(\Delta t) \rangle + \langle \delta u'^2_\sim(\Delta t) \rangle + \langle \delta u'^2_>(\Delta t) \rangle \tag{4.1}$$

FIGURE 18. (Colour online) Second-order structure functions of $u'_<$, $u'_\sim$ and $u'_>$ at (*a*) $X/T_0 = 6$ and (*b*) $X/T_0 = 26$ along the centreline. For comparison, the corresponding profile of u' is also plotted. From bottom to top, the three horizontal dashed lines indicate $2(U^<_{rms})^2$, $2(U^\sim_{rms})^2$ and $2(U^>_{rms})^2$. The vertical dashed lines correspond to half-vortex shedding cycle.

and

$$\langle \delta u'^2_\sim(\Delta t) \rangle = \langle \delta u'^2_{\sim,l}(\Delta t) \rangle + \langle \delta u'^2_{\sim,h}(\Delta t) \rangle. \tag{4.2}$$

A brief justification of the two equations can be found in supplementary appendix D. These two equations allow us to quantify the contribution of each velocity components, $u'_>$, $u'_\sim$ and $u'_<$, on the profile shape of $\langle \delta u'^2(\Delta t) \rangle$. Figure 18(*a*) implies that the discrepancy from the 2/3 scaling is probably associated with the strong vortex shedding. More specifically, for the time difference $\Delta t U_{in}/T_0 \simeq 3$, which defines the end of the 1 slope, the large-scale velocity components $u'_>$ make an overwhelming contribution to $\langle \delta u'^2(\Delta t) \rangle$.

At $X/T_0 = 6$ and 26, the second-order structure function of $u'_>$ acquire a well-defined 2 power-law scaling in the range $\Delta t U_{in}/T_0 \lesssim 3$. Moreover, the vortex shedding periods are more or less the same (see figures 11 and 17). That is, the time scales of $u'_>$ at $X/T_0 = 6$ and 26 are close to each other. Therefore, the stronger vortex shedding at $X/T_0 = 6$, as can be seen from the height of the oscillations in figure 18 and peak values of the spectra in figure 11, corresponds to a large coefficient $\langle (\partial u'(t)/\partial t)^2 \rangle$, which can significantly contaminate the profile of $\langle \delta u'^2(\Delta t) \rangle$ within the range $0.3 \lesssim \Delta t U_{in}/T_0 \lesssim 3$ (see figure 18*a*). In other words, fluid motions within this intermediate range are not sufficiently separated from large-scale motions and can directly 'feel' the large-scale vortex shedding. This observation violates Kolmogorov's universal equilibrium hypothesis. In the range $0.1 \lesssim \Delta t U_{in}/T_0 \lesssim 0.3$, however, the interpretation of the appearance of the approximate 1 power law should not be pushed too far since this exponent lies between the scaling law of 2/3 and 2. It is difficult to accurately compute the scaling law in the transition region between the 2/3 power-law range and the dissipation range with an exponent close 2. We again demonstrate that the −5/3 energy spectrum found at $X/T_0 = 6$ is not the well-known Kolmogorov −5/3 spectrum. On the other hand, at $X/T_0 = 26$, the occurrence of the 2/3 scaling of the second-order structure function along with the −5/3 energy spectrum appear to be in accord with the Kolmogorov phenomenology.

5. Conclusion

The streamwise evolutions of the statistical characteristics of turbulent flows behind two side-by-side square cylinders with different gap ratios (i.e. $L_d/T_0 = 4$, 6 and 8) are investigated by using DNSs. The wake-interaction length scale X_*, which is widely used to normalize the streamwise distance in the grid-generated turbulence, is explored in this paper. It is demonstrated that for the case with large gap ratios, in which two vortex streets are more persist, X_* can be used to describe the evolution of some important turbulence characteristics, at least to some extent.

To shed light on the formation mechanism of the extreme events, the turbulent flows at $X/T_0 = 6$ and 26 in the case with $L_d/T_0 = 6$ are extensively investigated. Our study confirms that the occurrences of the extreme events are associated with the large magnitude of v'. The energy spectrum at $X/T_0 = 6$, where turbulent flow is highly intermittent with the occurrence of the extreme events and undergoes transition to a fully turbulent state, acquires a well-defined $-5/3$ power law with a range for almost a decade. By extracting the velocity signals in the high-frequency region, we provide the first direct evidence that the occurrence of the well-known $-5/3$ power spectrum is directly attributed to the extreme events. In the intermediate-frequency range, both laminar and turbulent behaviours contribute to the formation of the $-5/3$ scaling law. In the downstream region $X/T_0 = 26$, however, the strength of the extreme events becomes weaker. Consequently, the range of the $-5/3$ energy spectrum narrows. The absence of the $2/3$ power law of the second-order structure function at $X/T_0 = 6$ finds its roots in the strong large-scale vortex shedding and the motions in the intermediate range can directly 'feel' the large-scale vortex shedding, which violates Kolmogorov's universal equilibrium hypothesis.

In this work, we prove that the extreme events and the $-5/3$ power-law scaling are closely related. Not limited to the dual-wake flow presented in this study, the appearance of the non-Kolmogorov $-5/3$ power-law scaling can also be found in the near field of various kinds of turbulent flows, as has already been reported. This work may open an avenue for understanding this phenomenon.

To investigate what physical mechanisms are responsible for the emergence of the $-5/3$ spectrum at $X/T_0 = 6$, we need to explore the corresponding scale-by-scale energy budget by resorting to the Kármán–Howarth–Monin–Hill equation, which is directly derived from the Navier–Stokes equations without making any assumptions and consequently can be used to study the energy transfer process in any kind of turbulence. Also, how the strong vortex shedding in the upstream region affects the energy cascade is another important topic, which should be pursued in future works.

Supplementary material

Supplementary material is available at https://doi.org/10.1017/jfm.2019.456.

REFERENCES

ALAM, M. M., BAI, H. L. & ZHOU, Y. 2016 The wake of two staggered square cylinders. *J. Fluid Mech.* **801**, 475–507.

ALAM, M. M. & ZHOU, Y. 2013 Intrinsic features of flow around two side-by-side square cylinders. *Phys. Fluids* **25**, 085106.

ALAM, M. M., ZHOU, Y. & WANG, X. W. 2011 The wake of two side-by-side square cylinders. *J. Fluid Mech.* **669**, 432–471.

FRISCH, U. 1995 *Turbulence: The Legacy of A. N. Kolmogorov*. Cambridge University Press.

GOMES-FERNANDES, R., GANAPATHISUBRAMANI, B. & VASSILICOS, J. C. 2012 Particle image velocimetry study of fractal-generated turbulence. *J. Fluid Mech.* **711**, 306–336.

GOMES-FERNANDES, R., GANAPATHISUBRAMANI, B. & VASSILICOS, J. C. 2014 Evolution of the velocity-gradient tensor in a spatially developing turbulent flow. *J. Fluid Mech.* **756**, 252–292.

HEARST, R. J. & LAVOIE, P. 2014 Scale-by-scale energy budget in fractal element grid-generated turbulence. *J. Turbul.* **15**, 540–554.

HURST, D. & VASSILICOS, J. C. 2007 Scalings and decay of fractal-generated turbulence. *Phys. Fluids* **19**, 035103.

ISAZA, J. C., SALAZAR, R. & WARHAFT, Z. 2014 On grid-generated turbulence in the near- and far field regions. *J. Fluid Mech.* **753**, 402–426.

KOLÁŘ, V., LYN, D. A. & RODI, W. 1997 Ensemble-averaged measurements in the turbulent near wake of two side-by-side square cylinders. *J. Fluid Mech.* **346**, 201–237.

KOLMOGOROV, A. N. 1941a Dissipation of energy in the locally isotropic turbulence. *Dokl. Akad. Nauk SSSR* **32**, 16–18.

KOLMOGOROV, A. N. 1941b The local structure of turbulence in incompressible viscous fluid for very large Reynolds numbers. *Dokl. Akad. Nauk SSSR* **30**, 301–305.

KOLMOGOROV, A. N. 1941c On the degeneration of isotropic turbulence in an incompressible viscous fluid. *Dokl. Akad. Nauk SSSR* **31**, 538–540.

KRAICHNAN, R. H. 1974 On Kolmogorov's inertial range theories. *J. Fluid Mech.* **62**, 305–330.

LAIZET, S. & LAMBALLAIS, E. 2009 High-order compact schemes for incompressible flows: a simple and efficient method with the quasi-spectral accuracy. *J. Comput. Phys.* **228**, 5989–6015.

LAIZET, S., LAMBALLAIS, E. & VASSILICOS, J. C. 2010 A numerical strategy to combine high-order schemes, complex geometry and parallel computing for high resolution dns of fractal generated turbulence. *Comput. Fluids* **39**, 471–484.

LAIZET, S. & LI, N. 2011 Incompact3d, a powerful tool to tackle turbulence problems with up to $O(10^5)$ computational cores. *Intl J. Numer. Meth. Fluids* **67**, 1735–1757.

LAIZET, S., NEDIĆ, J. & VASSILICOS, J. C. 2015a Influence of the spatial resolution on fine-scale features in dns of turbulence generated by a single square grid. *Intl J. Comput. Fluid Dyn.* **29**, 286–302.

LAIZET, S., NEDIĆ, J. & VASSILICOS, J. C. 2015b The spatial origin of $-5/3$ spectra in grid-generated turbulence. *Phys. Fluids* **27**, 065115.

LAIZET, S., VASSILICOS, J. C. & CAMBON, C. 2013 Interscale energy transfer in decaying turbulence and vorticity-strain-rate dynamics in grid-generated turbulence. *Fluid Dyn. Res.* **45**, 061408.

LELE, S. K. 1992 Compact finite difference schemes with spectral-like resolution. *J. Comput. Phys.* **103**, 16–42.

MAZELLIER, N. & VASSILICOS, J. C. 2010 Turbulence without Richardson–Kolmogorov cascade. *Phys. Fluids* **22**, 075101.

NAGATA, K., SAIKI, T., SAKAI, Y., ITO, Y. & IWANO, K. 2017 Effects of grid geometry on non-equilibrium dissipation in grid turbulence. *Phys. Fluids* **29**, 015102.

NAGATA, K., SAKAI, Y., INABA, T., SUZUKI, H., TERASHIMA, O. & SUZUKI, H. 2013 Turbulence structure and turbulence kinetic energy transport in multiscale/fractal-generated turbulence. *Phys. Fluids* **25**, 065102.

PARNAUDEAU, P., CARLIER, J., HEITZ, D. & LAMBALLAIS, E. 2008 Experimental and numerical studies of the flow over a circular cylinder at Reynolds number 3900. *Phys. Fluids* **20**, 085101.

PAUL, I., PAPADAKIS, G. & VASSILICOS, J. C. 2017 Genesis and evolution of velocity gradients in near-field spatially developing turbulence. *J. Fluid Mech.* **815**, 295–332.

PAUL, I., PAPADAKIS, G. & VASSILICOS, J. C. 2018 Evolution of passive scalar statistics in a spatially developing turbulence. *Phys. Rev. Fluids* **3**, 014612.

POPE, S. B. 2000 *Turbulent Flows*. Cambridge University Press.

PORTELA, F. A., PAPADAKIS, G. & VASSILICOS, J. C. 2017 The turbulence cascade in the near wake of a square prism. *J. Fluid Mech.* **825**, 315–352.

REDFORD, J. A., CASTRO, I. P. & COLEMAN, G. N. 2012 On the universality of turbulent axisymmetric wakes. *J. Fluid Mech.* **710**, 419–452.

DA SILVA, C. B., HUNT, J. C. R., EAMES, I. & WESTERWEEL, J. 2014 Interfacial layers between regions of different turbulence intensity. *Annu. Rev. Fluid Mech.* **46**, 567–590.

TENNEKES, H. & LUMLEY, J. L. 1972 *A First Course in Turbulence*. MIT Press.

TOWNSEND, A. A. 1956 *The Structure of Turbulent Shear Flows*. Cambridge University Press.

TRIAS, F. X., GOROBETS, A. & OLIVA, A. 2015 Turbulent flow around a square cylinder at Reynolds number 22,000: a DNS study. *J. Fluid Mech.* **123**, 87–98.

VALENTE, P. C. & VASSILICOS, J. C. 2011 The decay of turbulence generated by a class of multiscale grids. *J. Fluid Mech.* **687**, 300–340.

WILLIAMSON, C. H. K. 1996 Vortex dynamics in the cylinder wake. *Annu. Rev. Fluid Mech.* **28**, 477–539.

ZHENG, Q. & ALAM, M. M. 2017 Intrinsic features of flow past three square prisms in side-by-side arrangement. *J. Fluid Mech.* **826**, 996–1033.

ZHOU, Y., NAGATA, K., SAKAI, Y., ITO, Y. & HAYASE, T. 2015 On the evolution of the invariants of the velocity gradient tensor in single-square-grid-generated turbulence. *Phys. Fluids* **27**, 075107.

ZHOU, Y., NAGATA, K., SAKAI, Y., ITO, Y. & HAYASE, T. 2016a Enstrophy production and dissipation in developing grid-generated turbulence. *Phys. Fluids* **28**, 025113.

ZHOU, Y., NAGATA, K., SAKAI, Y., ITO, Y. & HAYASE, T. 2016b Spatial evolution of the helical behavior and the 2/3 power-law in single-square-grid-generated turbulence. *Fluid Dyn. Res.* **48**, 021404.

ZHOU, Y., NAGATA, K., SAKAI, Y., SUZUKI, H., ITO, Y., TERASHIMA, O. & HAYASE, T. 2014a Development of turbulence behind the single square grid. *Phys. Fluids* **26**, 045102.

ZHOU, Y., NAGATA, K., SAKAI, Y., SUZUKI, H., ITO, Y., TERASHIMA, O. & HAYASE, T. 2014b Relevance of turbulence behind the single square grid to turbulence generated by regular- and multiscale-grids. *Phys. Fluids* **26**, 075105.

ZHOU, Y., NAGATA, K., SAKAI, Y. & WATANABE, T. 2018 Dual-plane turbulent jets and their non-Gaussian velocity fluctuations. *Phys. Rev. Fluids* **3**, 124604.

ZHOU, Y., WANG, Z. J., XU, S. J. & JIN, W. 2001 Free vibrations of two side-by-side cylinders in a cross-flow. *J. Fluid Mech.* **443**, 197–229.